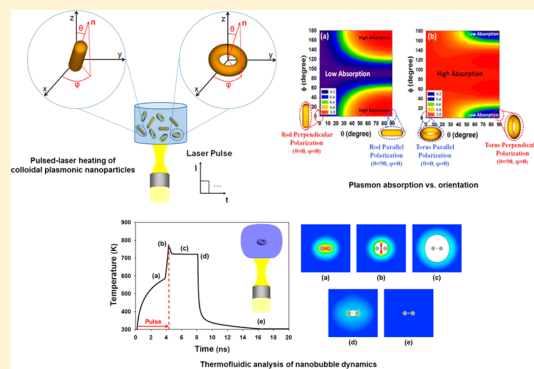


# Photonic and Thermofluidic Analysis of Colloidal Plasmonic Nanorings and Nanotori for Pulsed-Laser Photothermal Applications

Fatema Alali,<sup>†</sup> Ioannis H. Karamelas,<sup>‡</sup> Young Hwa Kim,<sup>†</sup> and Edward P. Furlani<sup>\*,†,‡</sup>

<sup>†</sup>Department of Electrical Engineering and <sup>‡</sup>Department of Chemical and Biological Engineering, University at Buffalo SUNY, Buffalo, New York 14260, United States

**ABSTRACT:** We propose the use of plasmonic nanorings and nanotori for enhanced colloidal photothermal energy conversion in the visible (vis) to near-infrared (NIR) spectrum. We use full-wave field analysis to demonstrate for the first time that the plasmon resonant absorption of these structures remains high over a broad range of orientations relative to the polarization of the incident field. The finding of strong orientation-independent plasmon absorption is a key result as it indicates that the structures can provide enhanced photothermal heating for colloidal applications. We use computational fluid dynamic analysis to investigate pulsed-laser plasmon-enhanced heating of the nanostructures in a fluid. We quantify the laser intensity and pulse duration needed to superheat the nanostructures to initiate bubble nucleation, and we simulate the dynamics of generated nanobubbles. The modeling provides insight into the plasmonic and thermofluidic behavior of colloidal nanostructures, thereby enabling rational design of novel plasmon-enhanced photothermal processes.



## 1. INTRODUCTION

Interest in nanoscale photothermal phenomena has grown steadily in recent years along with new applications in fields such as analytical and material chemistry, nanophotonics, and biomedicine. One of the most promising areas of research in this field involves the use of plasmonics wherein laser light is used to remotely heat subwavelength metallic (e.g., Au and Ag) nanoparticles. Such particles have unique optical properties that make them well suited for photothermal heating; most notably they exhibit localized surface plasmon resonance (LSPR). At plasmon resonance, there is a coherent oscillation of free electrons within the particles that gives rise to intense absorption and scattering of incident light as well as highly localized field enhancement. The absorbed photon energy is efficiently converted to heat, which is ultimately transferred to the surrounding medium. The LSPR of plasmonic nanoparticles occurs at shape- and size-dependent wavelengths that span the ultraviolet (UV) to near-infrared (NIR) spectrum. Moreover, a desired LSPR wavelength ( $\lambda_p$ ) can be obtained by controlling the size and shape of the particles during synthesis. The ability to tune  $\lambda_p$  and the associated resonant plasmonic effects have proven useful for applications that span the fields of biosensing, optical coherence tomography,<sup>1</sup> photoacoustic imaging,<sup>2</sup> and two-photon luminescence imaging,<sup>3</sup> among others. Two emerging biomedical applications that directly exploit plasmon-enhanced photothermal transduction are thermally modulated drug delivery<sup>4</sup> and photothermal cancer therapy.<sup>5,6</sup> Photothermal drug delivery has been demonstrated using plasmonic core-shell particles (37 nm gold sulfide core within a 4 nm gold shell) embedded within a thermally reversible polymer matrix.<sup>4</sup> A pulsed laser is used to heat the

particles at their plasmon resonant wavelength, which stimulates thermal release of “model drugs”, such as methylene blue or ovalbumin, from the nanoshell-composite hydrogels. The rate of drug release can be modulated using periodic laser irradiation, i.e., the rate increases when the laser is turned on and returns to a minimum level when the laser is off. The ability to modulate drug delivery could be used to optimize the release profile of therapeutic agents to match physiologic requirements of the patient. With regard to photothermal cancer therapy, plasmonic particles have been used in various modalities. One modality involves hyperthermia where gold nanoparticles are introduced into malignant tissue and heated using a pulsed laser to destroy the tissue by raising the local temperature 3–6 °C. More recently, an alternate therapy has emerged in which gold nanoparticles are uptaken by cancer cells and then pulsed with sufficient laser intensity to create bubbles within the cells that rupture their membrane. Lapotko et al. demonstrated the use of this technique for imaging and diagnosis as well as therapy at the cellular level.<sup>7–11</sup> They used laser-pulsed spherical (30 nm) gold nanoparticles to rupture K562 and human lymphoid leukemia cell membranes with minimal collateral damage to neighboring healthy cells.<sup>10</sup> Lukianova et al. also exploited plasmonic-generated nanobubbles for intracellular drug delivery.<sup>12,13</sup> Gold nanoparticles were used as drug carriers, and when they were irradiated with a pulsed laser, the nanobubbles that formed caused intracellular dispersal of the drug, which

Received: July 15, 2013

Revised: August 29, 2013

reduced the drug dosage and treatment time while increasing effectiveness.<sup>12</sup>

Most plasmon-based photothermal applications *in vivo* utilize gold nanoparticles that can be tuned to have an LSPR wavelength in the NIR (e.g., 800–1200 nm). The reason for this is that light at these wavelengths can pass through tissue with relatively little attenuation and be absorbed by the particles.<sup>14</sup> While various nanostructures can be designed to absorb in the NIR, to date, most *in vivo* studies have involved the use of three different particles, i.e., core-shell nanoparticles,<sup>15,16</sup> nanorods,<sup>17</sup> and nanocage structures.<sup>18–21</sup> These particles are attractive for such applications as they can be synthesized in a controllable fashion using bottom-up chemical methods. However, they also have drawbacks. Core-shell particles have relatively thin gold shells that limit absorption. Nanorods have more metallic mass, but their resonant NIR absorption is a strong function of their orientation relative to the polarization of the incident field, i.e., peak NIR absorption occurs when the rods are aligned parallel to the field polarization, but the absorption decreases dramatically as they rotate away from this orientation. Thus, colloidal nanorods with random orientations have reduced absorption, which results in less efficient heating. Gold nanocages can have relatively high absorption at arbitrary orientations, but they have less metallic mass than a solid particle, which limits their heat generation capability.

In this paper we propose the use of plasmonic nanorings and nanotori for enhanced photothermal colloidal heating applications (Figure 1). Various methods have been demonstrated for

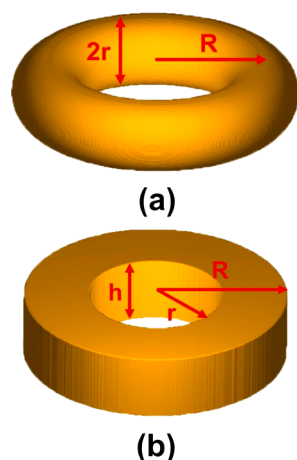


**Figure 1.** Nanostructures: (a) torus and (b) ring.

producing such particles.<sup>22,23</sup> Recently, they have been fabricated on substrates using top-down lithographic techniques and then released into a colloidal dispersion.<sup>24</sup> However, rapid advances in nanoparticle synthesis will likely lead to bottom-up methods for producing these particles in the near future. In addition, these structures can be tuned to have a high absorption cross-section in the NIR. We investigate photonic and photothermal aspects of these structures using a combination of computational electromagnetic and fluid dynamic (CFD) analysis as described by Furlani et al.<sup>25</sup> We use full-wave electromagnetic analysis to study plasmonic effects and compute the absorption spectra of these structures as a function of their orientation relative to the polarization of the incident field. We demonstrate for the first time that their absorption remains relatively high over a broad range of

orientations. This is a key result of this article, indicating that nanorings and nanotori are well suited for colloidal heating applications where they can obtain random orientations. These structures are superior to nanorods in this regard, and since they can contain more metallic mass than core-shell or nanocage particles, they should provide more efficient heating than those structures as well. We use CFD analysis to simulate nanosecond-pulsed laser heating of these structures in an aqueous medium. We quantify the intensity and duration of the laser pulse needed to superheat the structures to cause vaporization of the surrounding fluid leading to bubble nucleation. We simulate the entire photothermal process, i.e., temperature rise within the nanostructures, heat transfer to the surrounding fluid, phase change leading to bubble nucleation, and the dynamic behavior of the bubble and surrounding fluid during and after pulsed illumination. We demonstrate that plasmon-enhanced nanobubbles can, in principle, be generated in a controlled fashion without melting the plasmonic nanostructures. The combined electromagnetic and fluid dynamic modeling provides insight into fundamental aspects of the photothermal behavior of colloidal plasmonic nanorings and nanotori and their use for plasmon-enhanced heat transfer at the nanoscale. This analysis should prove useful for rational design of novel plasmon-enhanced photothermal processes.

## 2. PLASMONIC ANALYSIS

We use 3D full-wave time-harmonic field theory to study the absorption spectra of gold nanotori and nanorings as a function of their orientation relative to the polarization of an incident field. The plasmonic response of the particles depends on many factors including their aspect ratios, i.e.,  $r/R$  in the case of the nanotorus and  $(R - r)/R$  in the case of the nanoring. Estimates of their respective plasmon resonant wavelengths can be obtained using closed-form expressions that apply for a limited range of aspect ratios and for alignment parallel to the field as shown in Figure 2a.<sup>26,27</sup> Rigorous predictions on the plasmonic behavior for arbitrary geometries and orientations require numerical analysis. The finite element-based COMSOL RF solver ([www.comsol.com](http://www.comsol.com)) is used for this purpose. A typical computational domain is shown in Figure 2a. This contains a single Au nanotorus ( $R = 40$  nm,  $r = 10$  nm). Perfectly matched layers (PMLs) are applied at the top and bottom of the domain to reduce backscatter from these boundaries. Perfect electric conductor (PEC) conditions are applied at the boundaries perpendicular to  $\mathbf{E}$ , and perfect magnetic conductor (PMC) conditions are applied at the boundaries perpendicular to  $\mathbf{H}$ . These symmetry boundary conditions mimic the response of a 2D array of identical nanostructures with center-to-center  $x$  and  $y$  lattice spacing equal to the width of the computational domain in the  $x$  and  $y$  directions, respectively. The lattice spacing is chosen to be large enough so that the resulting predictions will reflect the response of essentially a single particle, i.e., negligible coupling with neighboring particles.

The particle is illuminated with a uniform downward-directed TEM plane wave with  $\mathbf{E}$  parallel to the  $x$  axis. The field satisfies the equation

$$\nabla \times (\mu_r^{-1} \nabla \times \mathbf{E}) - k_0^2 \left( \epsilon_r - j \frac{\sigma}{\omega \epsilon_0} \right) \mathbf{E} = 0 \quad (1)$$

where  $\mu_r$  and  $\epsilon_r$  are the relative permeability and permittivity of the media, respectively. For gold nanoparticles at optical frequencies,  $\mu_r = 1$  and  $\epsilon_r$  is modeled using an analytical

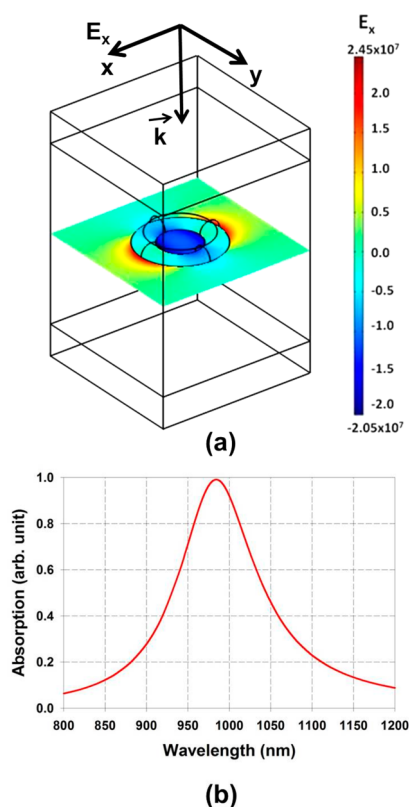


**Figure 2.** Photonic analysis of a nanotorus ( $R = 40$  nm,  $r = 10$  nm) with parallel alignment to the incident polarization: (a) computational domain and plot of  $E_x$  through a cross-section of the domain, (b) normalized absorbed power vs wavelength at parallel orientation.

expression that is based on a Drude–Lorentz model.<sup>25,28–30</sup> The fluid surrounding the nanoparticle is assumed to be nonabsorbing water with an index of refraction of  $n_f = 1.3$ . The incident field is generated by a time-harmonic surface current positioned in the  $x$ – $y$  plane directly below the upper PML.<sup>31,32</sup> The  $E$  field shown in Figure 3 reflects an induced low-order dipolar plasmon mode, i.e., the  $\mu = 1$  and  $\nu = 0$  mode described by Dutta et al. (see Figure 2 in ref 26). We compute the (wavelength-dependent) power absorbed by the particle  $Q_{\text{abs}}$

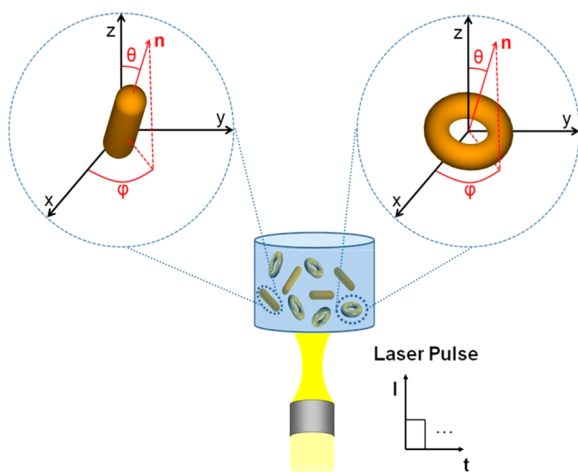


**Figure 3.** Pulsed laser heating of colloidal Au nanoparticles. Nanoparticle orientation is defined by angles  $\theta$  and  $\phi$ . (Inset) Laser pulse profile, irradiance  $I$  vs  $t$ .

(watts) (Figure 2b), which is converted to heat. Thus, this analysis predicts photothermal energy conversion within the particle.

### 3. PLASMONIC SIMULATIONS

In this section we compare photothermal energy conversion for colloidal nanorods and nanotori. In order to determine their heating efficiency, it is necessary to quantify their absorption as a function of orientation. The orientation can be specified using angles  $\phi$  and  $\theta$  that define the rotation of axis of the particle relative to the  $x$  and  $z$  axis, respectively. Figure 3 illustrates colloidal nanorods and nanotori being illuminated with a pulsed laser and a reference frame showing the angles  $\phi$  and  $\theta$  that define the orientation of the particles. Throughout this paper the incident field is assumed to be linearly polarized along the  $x$  axis and propagating downward with  $k$  in the  $-z$  direction as shown in Figure 2a. The inset plot in Figure 3 depicts the pulse profile (irradiance  $I$  vs  $t$ ) for the laser. In this figure,  $\mathbf{n}$  is the unit vector along the axis of the particle. For the nanorod,  $\mathbf{n}$  is along its length, whereas for a nanotorus,  $\mathbf{n}$  is along its axis of rotation. The angle  $\phi$  lies in the  $x$ – $y$  plane and is measured from the  $x$  axis to the projection of  $\mathbf{n}$  onto that plane, whereas  $\theta$  is the angle between  $\mathbf{n}$  and the  $z$  axis. As noted above, we assume that the incident field is linearly polarized along the  $x$  axis as shown in Figure 2a. As a point of reference, the torus in this figure has an orientation ( $\theta = 0^\circ$ ,  $\phi = 0^\circ$ ) and is aligned parallel to polarization, i.e., the  $E$  field is parallel to the face of the torus, perpendicular to its axis. The torus is aligned perpendicular to the polarization when ( $\theta = 90^\circ$ ,  $\phi = 0^\circ$ ) or ( $\theta = 90^\circ$ ,  $\phi = 90^\circ$ ). Similarly, a nanorod is said to be oriented parallel (longitudinal) to the polarization when ( $\theta = 90^\circ$ ,  $\phi = 0^\circ$ ) or perpendicular (transverse) when ( $\theta = 0^\circ$ ,  $\phi = 0^\circ$ ).

We first study the nanorod. It is well known that there are two distinct LSPR frequencies for this geometry that correspond to transverse and longitudinal polarization modes, respectively. A higher LSPR frequency (shorter wavelength) occurs for transverse alignment, whereas a lower resonant frequency (longer wavelength) is obtained for parallel alignment. Moreover, the latter depends on the aspect ratio (diameter/length) of the nanorod and can be tuned through synthesis for a specific application. The ability to tune LSPR in this fashion has spawned a growing interest in the use of gold nanorods, especially for bioapplications that require NIR wavelengths to achieve more effective penetration of light into a target tissue.

We model the nanorod as a cylinder with hemispherical caps. The length and diameter of the nanorod are 60 and 17 nm, respectively, which define an aspect ratio of 0.28. We compute the absorption spectra for five different orientations that range from parallel to transverse alignment in  $30^\circ$  increments: ( $\theta = 0^\circ$ ,  $\phi = 0^\circ$ ), ( $\theta = 30^\circ$ ,  $\phi = 30^\circ$ ), ( $\theta = 60^\circ$ ,  $\phi = 60^\circ$ ), ( $\theta = 90^\circ$ ,  $\phi = 90^\circ$ ), and ( $\theta = 90^\circ$ ,  $\phi = 0^\circ$ ). The normalized absorption spectra for these orientations are plotted in Figure 4a. The normalization is with respect to the peak absorption at parallel alignment. Note that as the nanorod rotates from parallel toward perpendicular alignment, the absorption decreases and the LSPR wavelength gradually shifts toward shorter wavelengths. These effects are nonlinear functions of the orientation and more pronounced the greater the rotation. Note that when the nanorod is aligned perpendicular to the polarization, i.e., for ( $\theta = 0^\circ$ ,  $\phi = 0^\circ$ ) and ( $\theta = 90^\circ$ ,  $\phi = 90^\circ$ ), the normalized absorption is greatly reduced and its amplitude needs to be plotted on a separate (left side) axis. Overall, this analysis shows



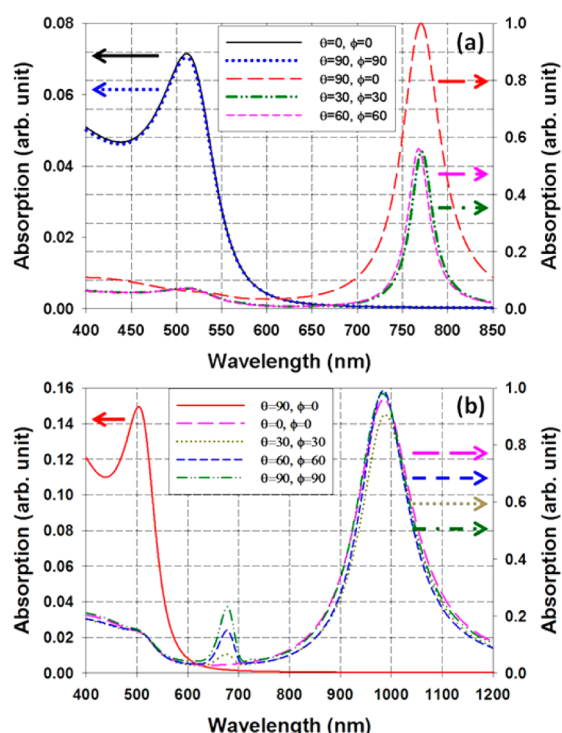


**Figure 4.** Normalized absorption spectra with nanoparticles at different orientations: (a) nanorod (length = 60 nm, diameter = 17 nm) and (b) nanotorus ( $R = 40$  nm,  $r = 10$  nm).

that when a colloid of nanorods is illuminated with the LSPR wavelength for parallel alignment, the absorbed power decreases substantially for misaligned nanorods, which reduces the overall colloidal heating efficiency.

We perform a similar analysis for the nanotorus. This geometry is defined by its major and minor radii,  $r$  and  $R$ , respectively, as shown in Figure 1a. The LSPR for the torus has been investigated using closed-form expressions<sup>26</sup> for both parallel alignment ( $\theta = 0^\circ$ ,  $\phi = 0^\circ$ ) (Figure 2a) and perpendicular alignment ( $\theta = 90^\circ$ ,  $\phi = 0^\circ$ ). We compute the absorption spectra for a nanotorus with  $R = 40$  nm and  $r = 10$  nm, i.e., with an aspect ratio of 0.25. As in the case of the nanorod, the resonant wavelength can be tuned to the NIR by adjusting the aspect ratio  $r/R$ . We determine the absorption spectra of the nanotorus for five different orientations, as above. These are plotted in Figure 4b. Note that in contrast to the nanorod, there is more overlap in the absorption spectra at different orientations and the LSPR wavelength first red shifts slightly and then blue shifts as the torus rotates away from parallel toward perpendicular alignment. This suggests that nanotori would provide more efficient colloidal heating than the nanorods due to their relatively higher absorption at different orientations.

We compare the absorption for these geometries over the full range of orientations, i.e.,  $0 \leq \theta \leq 90^\circ$  and  $0 \leq \phi \leq 180^\circ$ . This is a complex function of the geometry (especially the aspect ratio), the dielectric function of each particle, its orientation ( $\theta, \phi$ ), as well as the dielectric properties of the background medium. Numerical analysis is needed to study of these effects. We used full-wave analysis as described above to predict the normalized peak absorption contours at different orientations, as shown in Figure 5.

In this analysis, the nanorod and nanotori at different orientations are illuminated with their respective LSPR

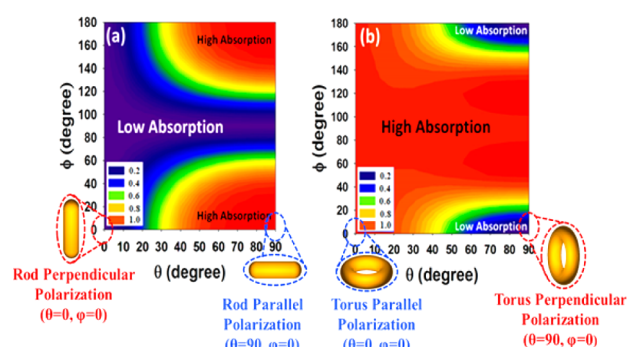


**Figure 5.** Normalized peak absorption at respective fixed LSPR wavelengths as a function of particle orientation ( $\theta, \phi$ ): (a) nanorod at  $\lambda = 770$  nm, (b) nanotorus at  $\lambda = 986$  nm ( $R = 40$  nm,  $r = 10$  nm).

wavelengths obtained for parallel orientation, in this case 770 and 986 nm, respectively. The idea is to determine the fall off in the peak absorption under a fixed illumination as the particles take on different orientations. Figure 5 clearly shows that the nanorod has a substantially decreased peak absorption at most orientations except for those nearly aligned with the polarization (e.g.,  $\theta = 90^\circ$ ,  $\phi = 0^\circ$ ). This is in sharp contrast to the nanotorus, which exhibits a relatively high peak absorption throughout a wide range of possible orientations (Figure 5b). The relatively high absorption by the nanotorus over an extended range of orientations is useful for photothermal applications involving colloidal particles.

#### 4. NANOTORI AND NANORINGS

Nanorings are closely related to nanotori in terms of their plasmonic behavior. An example of this can be seen in Figure 6,

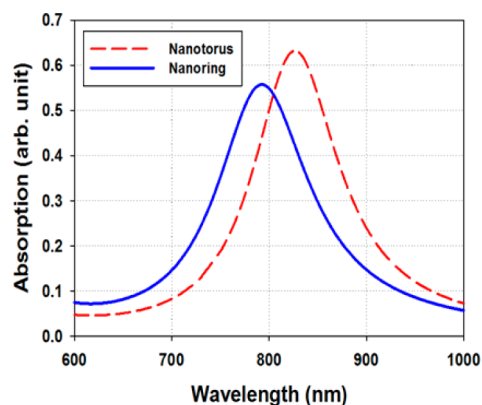


**Figure 6.** Absorption spectra for a nanoring ( $R = 40$  nm,  $r = 20$  nm,  $h = 20$  nm) and nanotorus ( $R = 30$  nm,  $r = 10$  nm), both aligned parallel to the incident field, i.e., with  $\theta = 0^\circ$ ,  $\phi = 0^\circ$ .

which shows the absorption spectra for the two geometries of comparable sizes when they are aligned parallel to the incident field, i.e., with  $\theta = 0^\circ$ ,  $\phi = 0^\circ$ . It is instructive to note that the resonant wavelength of the nanotorus is red shifted with respect to the nanoring. This is due primarily to the fact that the torus has a smaller aspect ratio ( $r/R = 1/3$ ) than the ring ( $(R - r)/R = 1/2$ ) (see Figure 2 and eq 30 in ref 26, eq 1 and Figure 3b in ref 27). Of the two structures, nanorings are currently easier to fabricate because their rectangular features can be realized using planar lithographic techniques. Au nanoring colloids have been

developed by first fabricating the structures on a substrate and then releasing them into solution.<sup>24</sup>

The normalized peak absorption vs orientation of nanorings is essentially the same as those of nanotori as shown in Figure 7. In this analysis the nanoring and nanotorus have comparable

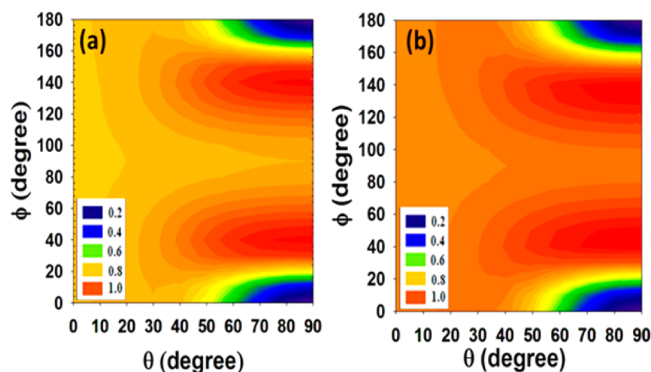


**Figure 7.** Normalized peak absorption at respective fixed LSPR wavelengths as a function of particle orientation ( $\theta$ ,  $\phi$ ): (a) nanoring at  $\lambda = 793$  nm ( $R = 40$  nm,  $r = 20$  nm), (b) nanotorus at  $\lambda = 825$  nm ( $R = 30$  nm,  $r = 10$  nm).

dimensions. The nanoring has inner and outer radii of 20 and 40 nm, respectively. All nanorings analyzed in the paper have a height of 20 nm. The nanotorus has the same dimensions as above,  $R = 30$  nm,  $r = 10$  nm. The nanoring and nanotorus at different orientations are illuminated with their respective LSPR wavelengths obtained for a parallel orientation, i.e., 793 and 825 nm, respectively. Specifically, these wavelengths are held constant as the particle orientations change. The analysis shown in Figures 6 and 7 indicates that nanorings and nanotori can be essentially interchanged for photothermal applications. In the following section, we analyze photothermal heating of these particles in fluid.

## 5. THERMOFLUIDIC ANALYSIS

We use CFD analysis to study the thermofluidic behavior of laser-heated nanoparticles in fluid. This is a complex process in which nonequilibrium thermal effects take place at femto- to picosecond time scales.<sup>33</sup> A discussion of the validity of our approach at the nanoscale can be found in our previously published work.<sup>25</sup> The FLOW-3D program (www.flow3d.com) is used for this analysis. This program is based on the volume of fluid (VOF) method, which is implemented using a finite-difference numerical scheme.<sup>34</sup> In the computational model, the nanostructures are immersed in an incompressible Newtonian fluid with a surface tension  $\sigma$ , viscosity  $\mu$ , density  $\rho$ , specific heat at constant pressure  $c_p$ , and thermal conductivity  $k$ . These properties are assumed to be constant and taken to be those of water at 300 K. The equations governing heat and mass transfer are as follows.

Navier–Stokes

$$\rho \left( \frac{\partial \mathbf{v}}{\partial t} + \mathbf{v} \cdot \nabla \mathbf{v} \right) = -\nabla p + \mu \nabla^2 \mathbf{v} \quad (2)$$

Incompressibility

$$\nabla \cdot \mathbf{v} = 0 \quad (3)$$

Heat transfer

$$\rho c_p \left( \frac{\partial T}{\partial t} + \mathbf{v} \cdot \nabla T \right) = k \nabla^2 T \text{ (fluid)} \quad (4)$$

$$\rho_{np} c_{np} \frac{\partial T_{np}}{\partial t} = Q_{abs}(t) + k_{np} \nabla^2 T_{np} \text{ (nanoparticle)} \quad (5)$$

In the equations  $\mathbf{v}$  and  $p$  are the velocity and pressure in the fluid and  $\rho_{np}$ ,  $c_{np}$ , and  $k_{np}$  are the density, specific heat at constant pressure, and thermal conductivity of the nanoparticle, respectively.  $Q_{abs}$  is the power generated uniformly within by the nanoparticle due to absorption of incident laser light, and  $T$  and  $T_{np}$  are the corresponding temperatures in the fluid and the nanoparticle. We model the gold nanoparticles using the following properties:  $\rho_{gold} = 19\,300$  kg/m<sup>3</sup>,  $c_{gold} = 129$  J/kg·K, and  $k_{gold} = 317$  W/m·K.

If the nanostructure reaches a sufficiently high “superheat” temperature the fluid at its surface undergoes a phase change (vaporization) that initiates bubble nucleation. This is taken to be 580 K for H<sub>2</sub>O. Before nucleation, the temperature in the particle and surrounding fluid is calculated using eqs 4 and 5. Once a bubble is nucleated, its interface is computed using the VOF method. The pressure in the bubble is initially set to the saturation pressure at the superheat temperature (approximately 100 atm), which is computed using the Clausius–Clayperon equation

$$p_{sat}(T) = p_1 \exp \left[ \frac{\Delta H_{vap}}{R} \left( \frac{1}{T_1} - \frac{1}{T} \right) \right] \quad (6)$$

where  $p_1$  and  $T_1$  are the pressure and temperature at a point on the saturation curve (e.g.,  $p_1 = 100$  kPa,  $T_1 = 273$  K),  $\Delta H_{vap}$  ( $40.65 \times 10^3$  J/mol) is the molar enthalpy of vaporization, and  $R$  (8.314 J/mol·K) is the universal gas constant. This pressure exerts an outward force at the liquid–bubble interface that causes it to expand outward from the particle. As the bubble grows, the pressure  $p_{vap}$ , temperature  $T_{vap}$ , and density  $\rho_{vap}$  of the vapor within it are computed using the equation-of-state of an ideal gas

$$p_{vap} = (\gamma - 1) \rho_{vap} C_{vap,v} T_{vap} \quad (7)$$

where  $c_{vap}$  is the specific heat of the vapor at constant volume and  $\gamma = c_{vap,p}/c_{vap,v}$  is the ratio of specific heats. The pressure, temperature, and density are assumed to be spatially uniform (i.e., homogeneous) within the bubble. The mass flux  $\dot{m}$  at the fluid–bubble interface is proportional to the deviation of the fluid from its saturation conditions, i.e.

$$\dot{m} = \sqrt{\frac{MW}{2\pi R}} \left( c_{evap} \frac{p_l^{sat}}{\sqrt{T_l}} - c_{cond} \frac{p_{vap}}{\sqrt{T_{vap}}} \right) \quad (8)$$

where  $MW$  is the molecular weight of the vapor,  $R$  is the vapor gas constant,  $T$  is temperature (K), and the subscripts  $l$  and  $v$  refer to liquid and vapor phases, respectively. The term  $p_l$  is the saturation pressure corresponding to the liquid temperature  $T_l$ , and  $c_{evap}$  and  $c_{cond}$  are accommodation coefficients for evaporation and condensation.

After the bubble has nucleated, the nanoparticle is surrounded by vapor and the heat transfer at the particle–vapor interface is greatly diminished. Thus, if the laser pulse continues beyond nucleation, the temperature of the essentially insulated nanoparticle rises rapidly and can reach its melting or even vaporization temperature within a nanosecond or less. For

**Table 1. Summary of Nanoring and Nanotorus Geometries with Heating and Nanobubble Parameters**

nanoparticle type	radius dimensions (nm)	power ( $\mu$ W)	pulse duration (ns)	laser irradiance ( $\text{mW}/\mu\text{m}^2$ ) ( $\lambda$ nm)	maximum nanoparticle temperature (K)	maximum bubble radius (nm)	nucleation time (ns)	maximum bubble time (ns)
nanoring ( $h = 20$ nm)	$R = 50, r = 30$	252	4	27.07 (935)	862	95	3.5	6.3
	$R = 40, r = 20$	192	3.8	11.79 (793)	984	85	3.2	5.5
	$R = 30, r = 10$	127.2	4.1	6.94 (662)	972	50	3.5	4.8
nanotorus	$R = 40, r = 10$	259.2	3.1	21.82 (986)	889	70	2.7	4.9
	$R = 30, r = 10$	172.8	4.1	10.06 (825)	1000	80	3.4	5.4
	$R = 20, r = 10$	115.2	4.1	7.94 (680)	773	65	3.7	5.6

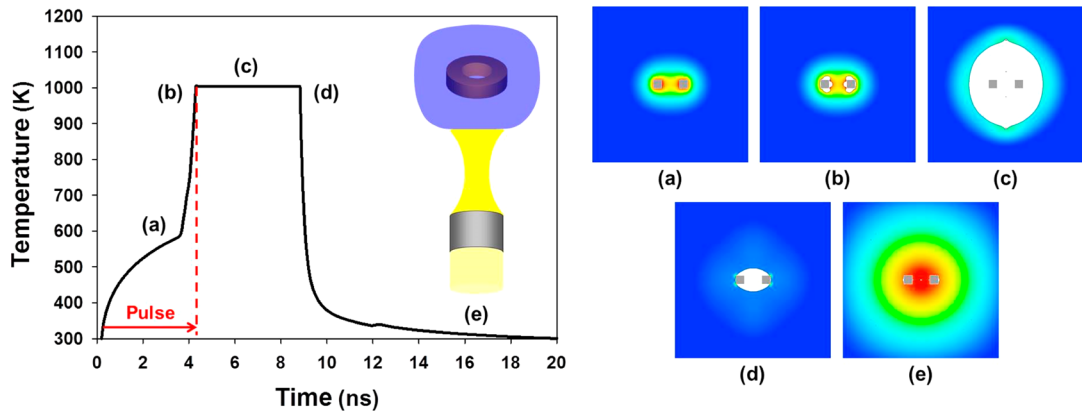


**Figure 8.** Photothermal heat cycle of a nanoring ( $R = 40$  nm,  $r = 20$  nm; cross-sectional view): plot of nanoring temperature vs time, pulse duration indicated by red arrow and dashed line, and inset plots showing various phases of the thermal cycle; (a) initial heating, (b) nanobubble formation, (c) nanobubble (maximum size), (d) nanobubble collapse, (e) cooling.

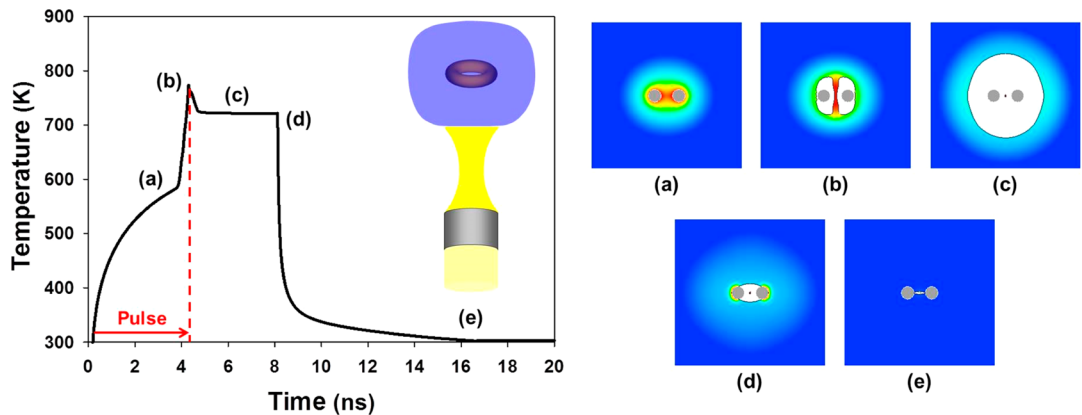


**Figure 9.** Photothermal heat cycle of a nanotorus ( $R = 20$  nm,  $r = 10$  nm; cross-sectional view): plot of nanotorus temperature vs time, pulse duration indicated by red arrow and dashed line, and inset plots showing various phases of the thermal cycle; (a) initial heating, (b) nanobubble formation, (c) nanobubble (maximum size), (d) nanobubble collapse, (e) cooling.

bulk gold, these values are  $T_m = 1336$  K and  $T_{\text{vap}} = 2933$  K, respectively. However, experiments have shown that Au nanoparticles have a lower melting point that can differ by as much as 200 K from the bulk value.<sup>35,36</sup> In order to avoid high-temperature damage to the particle, the laser power level and pulse duration must be carefully controlled. We use modeling to determine values of these parameters that keep the nanoparticle below a maximum temperature of 1100 K.

## 6. THERMOFLUIDIC SIMULATIONS

CFD simulations were performed to study the pulsed photothermal cycle of various gold nanoring and nanotorus geometries as defined in Table 1. The analysis was divided into two phases. In the first phase, we predicted the power level required to heat the nanoparticles from an ambient temperature

of 300 K to the superheat temperature of 580 K. This depends on the pulse duration, which was constrained in all cases to be between 3 to 5 ns. This time scale far exceeds the characteristic time constants for nonequilibrium energy transfer mechanisms that occur in laser-pulsed gold nanoparticles and are therefore consistent with the continuum modeling approach taken here.<sup>25</sup> In the second phase of the analysis we applied the power levels obtained in phase one and increased the pulse duration so that the nanoparticles were heated beyond the superheat temperature, which caused vaporization of the surrounding fluid and bubble nucleation. The pulse duration was tuned so that the nanoparticle achieved a temperature that was sufficiently high to generate a sustained nanobubble but low enough ( $<1100$  K) to avoid melting the nanoparticle.

A summary of key simulation parameters is given in Table 1. Figures 8 and 9 illustrate representative simulation results for the mid-sized nanoring ( $R = 40$  nm,  $r = 20$  nm) and the small nanotorus ( $R = 20$  nm,  $r = 10$  nm), respectively. These figures show a plot of the nanoparticle temperature vs time and inset pictures of the particle and the fluid temperature at various phases of the thermal cycle. Initially, the nanoparticles and fluid are at the ambient temperature 300 K. The heat pulse starts after 0.2 ns, causing a gradual rise in the temperature of the nanoparticle, which is indicated in plot segment and inset plot a. This continues until the nanoparticle reaches the superheat temperature, at which point a homogeneous bubble is nucleated around it. Upon nucleation, a thin sheath of vapor surrounds the nanoparticle and partially insulates it. Since power is still being dissipated in the nanoparticle, its temperature rises rapidly. This continues until the end of the heat pulse, which coincides with a maximum temperature as shown in plot segment and inset plot b. The pulse duration for the nanoring and nanotorus are 3.8 and 4.1 ns, respectively, as listed in Table 1 and indicated by a red dashed line. As soon as the nanobubble forms, it expands due to its high pressure relative to the surrounding fluid.<sup>25</sup> The nanobubble reaches a maximum size as shown in inset plot c. The maximum bubble radius for each geometry is given in Table 1. Subsequently, the bubble contracts and collapses, bringing fluid back in contact with the nanoparticle as shown in plot segment and inset plot d. The nanoparticle gradually cools to ambient temperature as more of the fluid comes in contact with it as shown in plot segment and inset plot e. An interesting observation of this process is formation of a hot droplet of fluid in the middle of the nanoparticle, which in some cases evaporates as the nanobubble expands.

The CFD simulations were performed on a Hex-core workstation with 32 GB of RAM. An axisymmetric computational domain with a uniform 1 nm mesh was used for all calculations. The computational domain extended 200 nm in both the  $r$  and the  $z$  directions for all but one of the geometries, i.e., the small nanotorus ( $R = 20$  nm,  $r = 10$  nm). We found that this geometry required a slightly larger domain that extended 300 and 260 nm in the  $r$  and  $z$  directions, respectively, to suppress numerical instabilities caused by a rapidly expanding nanobubble. Symmetry boundary conditions were imposed along the  $r$  and  $z$  axes, and the conditions  $P = 1$  atm ( $10^5$  Pa) and  $T = 300$  K were imposed on all boundaries. These were also the initial conditions set throughout the computational domain. The time for the simulations varied from 8 to 18 h depending on the geometry.

## 7. DISCUSSION

We performed photonic analysis to determine the absorption spectra of nanorings and nanotori as a function of their orientation and thermofluidic analysis to determine the absorbed power and pulse duration needed to heat the nanoparticles to create sustained nanobubbles. It remains to determine the laser irradiance needed to produce the required absorbed power within the nanoparticles, which depends on their orientation. Without loss of generality, we perform this calculation for the case of an aligned nanoring. We assume that a colloid of these particles will be illuminated at the LSPR wavelength for parallel alignment. From the photonic analysis, we can compute the laser irradiance needed to produce a given absorbed power. For example, for the mid-sized nanoring (Figure 8), we find that an irradiance of  $I_{\text{inc}} = 11.79$  mW/ $\mu\text{m}^2$

at the LSPR wavelength of  $\lambda = 793$  nm will produce the required absorbed power of 192  $\mu\text{W}$ . The corresponding values for different geometries of nanorings and nanotori at parallel alignment are listed in Table 1. The irradiance needed for an arbitrary orientation can be computed in a similar fashion.

Another consideration for plasmon-based photothermal applications is the impact of imperfections in particle shape or a dispersion of particle size on the absorption spectra. While it is not possible to quantify this impact absent a rigorous parametric photonic analysis, it can be estimated using closed-form expressions to predict the change in the resonant frequency  $\omega_p$  of the lowest order dipolar mode as a function of geometric variations. For the torus in free space,  $\omega_p$  can be estimated using

$$\omega_p = \omega_B \sqrt{\frac{r}{R} I_0' \left( \frac{r}{R} \right) K_0 \left( \frac{r}{R} \right)} \quad (9)$$

where  $\omega_B$  is the bulk plasmon frequency and  $I_0$  and  $K_0$  are modified Bessel functions of order 0.<sup>26</sup> From eq 9 we find that  $\omega_p$  decreases (i.e.,  $\lambda_p$  red shifts) in a nonlinear fashion as the aspect ratio  $r/R$  decreases as shown in Figure 10. As  $\lambda_p$  red

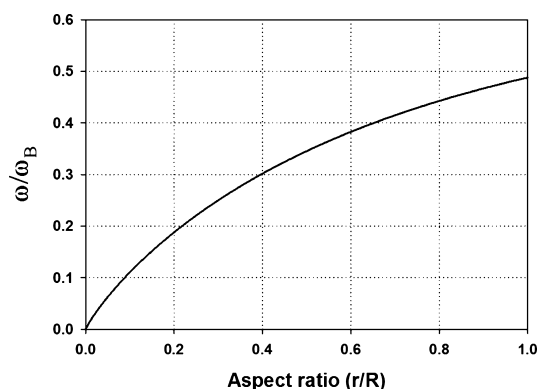


**Figure 10.** Normalized plasmon resonant frequency vs aspect ratio for a subwavelength nanotorus in free space at parallel orientation.

shifts relative to the illumination wavelength, i.e., the LSPR wavelength determined for an ideal particle, the absorption and hence photothermal heating efficiency decrease. Thus, eq 9 can be used to at least estimate the relative decrease in absorption and heating for limited variations in the size and shape of colloidal particles. A similar expression and analysis applies for nanorings (see eq 1 and Figure 3b in ref 27).

## 8. CONCLUSIONS

We used computational modeling to demonstrate that colloidal plasmonic nanorings and nanotori have advantageous absorption properties for photothermal applications. Their resonant absorption can be tuned to NIR wavelengths, and their level of absorption remains relatively high over a broad range of orientations relative to the polarization of the incident field. These properties hold potential for applications such as photothermal cancer therapy as they can enable more efficient heating of malignant tissue and access to deeper tumors. A more detailed analysis of the therapeutic potential of the nanoparticles is the focus of our ongoing research. Lastly, the computational approach demonstrated in this paper, i.e., combined photonic and thermofluidic analysis, provides insight into fundamental aspects of the photothermal process and enables rational design for novel applications.



## AUTHOR INFORMATION

### Corresponding Author

\*Phone: (716) 645-1194. Fax: (716) 645-3822. E-mail: efurlani@buffalo.edu.

### Author Contributions

This manuscript was written through contributions of all authors. All authors have given approval to the final version of the manuscript. All authors contributed equally.

### Notes

The authors declare no competing financial interest.

## REFERENCES

- (1) Oldenburg, A. L.; Hansen, M. H.; Zweifel, D. A.; Wei, A.; Boppart, S. A. Plasmon-Resonant Gold Nanorods as Low Back-scattering Albedo Contrast Agents for Optical Coherence Tomography. *Opt. Express* **2006**, *14*, 6724–6738.
- (2) Agarwal, A.; Huang, S. W.; Odonnell, M.; Day, K. C.; Day, M.; Kotov, N.; Ashkenazi, S. Targeted Gold Nanorod Contrast Agent for Prostate Cancer Detection by Photoacoustic Imaging. *J. Appl. Phys.* **2007**, *102* (6), 064701–064701–4.
- (3) Wang, H.; Huff, T. B.; Zweifel, D. A.; He, W.; Low, P. S.; Wei, A.; Cheng, J.-X. In Vitro and in Vivo Two-Photon Luminescence Imaging of Single Gold Nanorods. *Proc. Natl. Acad. Sci. U.S.A.* **2005**, *102* (44), 15752–15756.
- (4) Serksen, S. R.; Westcott, S. L.; Halas, N. J.; West, J. L. Temperature-Sensitive Polymer–Nanoshell Composites for Photo-thermally Modulated Drug Delivery. *J. Biomed. Mater. Res.* **2000**, *51* (3), 293–298.
- (5) Hirsch, L. R.; Stafford, R. J.; Bankson, J. A.; Serksen, S. R.; Rivera, B.; Price, R. E.; Hazle, J. D.; Halas, N. J.; West, J. L. Nanoshell-Mediated Near-Infrared Thermal Therapy of Tumors under Magnetic Resonance Guidance. *Proc. Natl. Acad. Sci.* **2003**, *100* (23), 13549–13554.
- (6) Dickerson, E. B.; Dreaden, E. C.; Huang, X.; El-Sayed, I. H.; Chu, H.; Pushpanketh, S.; McDonald, J. F.; El-Sayed, M. A. Gold Nanorod Assisted Near-Infrared Plasmonic Photothermal Therapy (PPTT) of Squamous Cell Carcinoma in Mice. *Cancer Lett.* **2008**, *269* (1), 57–66.
- (7) Lapotko, D. Plasmonic Nanoparticle-Generated Photothermal Bubbles and Their Biomedical Applications. *Nanomedicine* **2009**, *4* (7), 813–845.
- (8) Lapotko, D. Optical Excitation and Detection of Vapor Bubbles Around Plasmonic Nanoparticles. *Opt. Express* **2009**, *17* (4), 2538–2556.
- (9) Lapotko, D. O.; Lukianova, E.; Oraevsky, A. A. Selective Laser Nano-Thermolysis of Human Leukemia Cells with Microbubbles Generated Around Clusters of Gold Nanoparticles. *Lasers Surg. Med.* **2006**, *38* (6), 631–642.
- (10) Lapotko, D.; Lukianova, E.; Potapnev, M.; Aleinikova, O.; Oraevsky, A. Method of Laser Activated Nano-Thermolysis for Elimination of Tumor Cells. *Cancer Lett.* **2006**, *239* (1), 36–45.
- (11) Lapotko, D. Pulsed Photothermal Heating of the Media During Bubble Generation Around Gold Nanoparticles. *Int. J. Heat Mass Transfer* **2009**, *52* (5–6), 1540–1543.
- (12) Lukianova-Hleb, E. Y.; Belyanin, A.; Kashinath, S.; Wu, X.; Lapotko, D. O. Plasmonic Nanobubble-Enhanced Endosomal Escape Processes for Selective and Guided Intracellular Delivery of Chemotherapy to Drug-Resistant Cancer Cells. *Biomaterials* **2012**, *33* (6), 1821–1826.
- (13) Lukianova-Hleb, E. Y.; Koneva, I. I.; Oginsky, A. O.; La Francesca, S.; Lapotko, D. O. Selective and Self-Guided Micro-Ablation of Tissue with Plasmonic Nanobubbles. *J. Surg. Res.* **2011**, *166* (1), e3–e13.
- (14) Simpson, C. R.; Kohl, M.; Essenpreis, M.; Cope, M. Near-Infrared Optical Properties of Ex Vivo Human Skin and Subcutaneous Tissues Measured Using the Monte Carlo Inversion Technique. *Phys. Med. Biol.* **1998**, *43* (9), 2465.
- (15) Oldenburg, S. J.; Averitt, R. D.; Westcott, S. L.; Halas, N. J. Nanoengineering of Optical Resonances. *Chem. Phys. Lett.* **1998**, *288* (2–4), 243–247.
- (16) Harris, N.; Ford, M. J.; Mulvaney, P.; Cortie, M. B. Tunable Infrared Absorption by Metal Nanoparticles: the Case for Gold Rods and Shells. *Gold Bull.* **2008**, *41*, 5.
- (17) Gou, L.; Murphy, C. J. Fine-Tuning the Shape of Gold Nanorods. *Chem. Mater.* **2005**, *17* (14), 3668–3672.
- (18) Chen, J.; Glaus, C.; Laforest, R.; Zhang, Q.; Yang, M.; Gidding, M.; Welch, M. J.; Xia, Y. Gold Nanocages as Photothermal Transducers for Cancer Treatment. *Small* **2010**, *6* (7), 811–817.
- (19) Sun, Y.; Xia, Y. Mechanistic Study on the Replacement Reaction between Silver Nanostructures and Chloroauric Acid in Aqueous Medium. *J. Am. Chem. Soc.* **2004**, *126* (12), 3892–3901.
- (20) Chen, J.; McLellan, J. M.; Siekkinen, A.; Xiong, Y.; Li, Z.-Y.; Xia, Y. Facile Synthesis of Gold–Silver Nanocages with Controllable Pores on the Surface. *J. Am. Chem. Soc.* **2006**, *128* (46), 14776–14777.
- (21) Skrabalak, S. E.; Chen, J.; Sun, Y.; Lu, X.; Au, L.; Cobley, C. M.; Xia, Y. Gold Nanocages: Synthesis, Properties, and Applications. *Acc. Chem. Res.* **2008**, *41* (12), 1587–1595.
- (22) Zinchenko, A. A.; Yoshikawa, K.; Baigl, D. DNA-Templated Silver Nanorings. *Adv. Mater.* **2005**, *17*, 2820–2823.
- (23) Yan, F.; Goedel, W. A. Preparation of Mesoscopic Gold Rings Using Particle Imprinted Templates. *Nano Lett.* **2004**, *4* (7), 1193–1196.
- (24) Lee, C.-K.; Tseng, H.-Y.; Lee, C.-Y.; Wu, S.-Y.; Chi, T.-T.; Yang, K.-M.; Chou, H.-Y. E.; Tsai, M.-T.; Wang, J.-Y.; Kiang, et al. Characterizing the Localized Surface Plasmon Resonance Behaviors of Au Nanorings and Tracking Their Diffusion in Bio-Tissue with Optical Coherence Tomography. *Biomed. Opt. Express* **2010**, *1* (4), 1060–1074.
- (25) Furlani, E. P.; Karampelas, I. H.; Xie, Q. Analysis of Pulsed Laser Plasmon-Assisted Photothermal Heating and Bubble Generation at the Nanoscale. *Lab Chip* **2012**, *12* (19), 3707–3719.
- (26) Dutta, C. M.; Ali, T. A.; Brandl, D. W.; Park, T.-H.; Nordlander, P. Plasmonic Properties of a Metallic Torus. *J. Chem. Phys.* **2008**, *129* (8), 084706–9.
- (27) Aizpurua, J.; Hanarp, P.; Sutherland, D. S.; Kall, M.; Bryant, G. W.; de Abajo, F. J. G. Optical Properties of Gold Nanorings. *Phys. Rev. Lett.* **2003**, *90*, 057401.
- (28) Etchegoin, P. G.; Le Ru, E. C.; Meyer, M. An Analytic Model for the Optical Properties of Gold. *J. Chem. Phys.* **2006**, *125* (16), 164705–3.
- (29) Etchegoin, P. G.; Le Ru, E. C.; Meyer, M. Erratum: An Analytic Model for the Optical Properties of Gold. *J. Chem. Phys.* **2006**, *125*, 164705. et al. *J. Chem. Phys.* **2007**, *127* (18), 189901–1.
- (30) Johnson, P. B.; Christy, R. W. Optical Constants of the Noble Metals. *Phys. Rev. B* **1972**, *6* (12), 4370–4379.
- (31) Furlani, E. P.; Baev, A. Optical Nanotrapping Using Cloaking Metamaterial. *Phys. Rev. E* **2009**, *79* (2), 026607.
- (32) Furlani, E. P.; Baev, A. Free-Space Excitation of Resonant Cavities Formed from Cloaking Metamaterial. *J. Mod. Opt.* **2009**, *56* (4), 523–529.
- (33) Hu, M.; Hartland, G. V. Heat Dissipation for Au Particles in Aqueous Solution: Relaxation Time versus Size. *J. Phys. Chem. B* **2002**, *106*, 7029–7033.
- (34) Hirt, C. W.; Nichols, B. D. Volume of Fluid (VOF) Method for the Dynamics of Free Boundaries. *J. Comput. Phys.* **1981**, *39* (1), 201–225.
- (35) Inasawa, S.; Sugiyama, M.; Yamaguchi, Y. Laser-Induced Shape Transformation of Gold Nanoparticles below the Melting Point: The Effect of Surface Melting. *J. Phys. Chem. B* **2005**, *109* (8), 3104–3111.
- (36) Petrova, H.; Perez Juste, J.; Pastoriza-Santos, L.; Hartland, G. V.; Liz-Marzan, L. M.; Mulvaney, P. On the Temperature Stability of Gold Nanorods: Comparison Between Thermal and Ultrafast Laser-Induced Heating. *Phys. Chem. Chem. Phys.* **2006**, *8* (7), 814–821.